

## A POSSIBLY UNIVERSAL RED CHROMOPHORE FOR MODELING COLOR VARIATIONS ON JUPITER

L. A. SROMOVSKY<sup>1</sup>, K. H. BAINES<sup>1</sup>, P. M. FRY<sup>1</sup>, R. W. CARLSON<sup>2</sup>

<sup>1</sup>Space Science and Engineering Center, University of Wisconsin-Madison, 1225 West Dayton Street, Madison, WI 53706, USA and  
<sup>2</sup>Jet Propulsion Laboratory, 4800 Oak Grove Drive, Pasadena, CA 91109, USA

*Journal reference: Icarus 291 (2017) 232-244*

### ABSTRACT

A new laboratory-generated chemical compound made from photodissociated ammonia (NH<sub>3</sub>) molecules reacting with acetylene (C<sub>2</sub>H<sub>2</sub>) was suggested as a possible coloring agent for Jupiter's Great Red Spot (GRS) by Carlson et al. (2016, Icarus 274, 106-115). Baines et al. (2016, Icarus, submitted) showed that the GRS spectrum measured by the visual channels of the Cassini VIMS instrument in 2000 could be accurately fit by a cloud model in which the chromophore appeared as a physically thin layer of small particles immediately above the main cloud layer of the GRS. Here we show that the same chromophore and same layer location can also provide close matches to the short wave spectra of many other cloud features on Jupiter, suggesting this material may be a nearly universal chromophore that could explain the various degrees of red coloration on Jupiter. This is a robust conclusion, even for 12% changes in VIMS calibration and large uncertainties in the refractive index of the main cloud layer due to uncertain fractions of NH<sub>4</sub>SH and NH<sub>3</sub> in its cloud particles. The chromophore layer can account for color variations among north and south equatorial belts, equatorial zone, and the Great Red Spot, by varying particle size from 0.12 μm to 0.29 μm and 1-μm optical depth from 0.06 to 0.76. The total mass of the chromophore layer is much less variable, ranging from 18 to 30 μg/cm<sup>2</sup>, except in the equatorial zone, where it is only 10-13 μg/cm<sup>2</sup>. We also found a depression of the ammonia volume mixing ratio in the two belt regions, which averaged 0.4-0.5 × 10<sup>-4</sup> immediately below the ammonia condensation level, while the other regions averaged twice that value.

*Subject headings:* Jupiter; Jupiter, Atmosphere; Jupiter, Clouds

### 1. INTRODUCTION

It has long been known that the condensable molecules near the visible cloud level in Jupiter's atmosphere, including ammonia and ammonium hydrosulfide, are colorless at visible wavelengths, while Jupiter's cloud features have an overall red coloration to varying degrees, as evident from the spectral samples shown in Fig. 1. Jupiter's clouds presumably contain some unknown compound that absorbs blue light preferentially, with the Great Red Spot being a region of enhanced red coloration. A number of suggestions have been made over the years to explain the color of the GRS, including molecules involving nitrogen, sulfur, phosphorous, and various compounds generated by irradiation, and complex organics of unknown composition such as tholins, as summarized by West et al. (1986) and further reviewed by West et al. (2009). Recent arguments have been advanced for irradiated NH<sub>4</sub>SH by Loeffler et al. (2016). Until recently no accurate match to the GRS spectrum had ever been demonstrated. Judging on the basis of spectral fit quality, the most promising material suggested as the GRS coloring agent is a laboratory-generated chemical compound made from photodissociated ammonia (NH<sub>3</sub>) molecules reacting with acetylene (C<sub>2</sub>H<sub>2</sub>), described by Carlson et al. (2016). Baines et al. (2016) showed that the GRS spectrum measured by the visual channels of the Cassini VIMS instrument in 2000 could be accurately fit by a cloud model in which the chromophore appeared as a physically thin layer of small chromophore particles immediately above the main cloud layer of the GRS, which they referred to as the crème brûlée model because of the dessert's analogous verti-

cal structure. They also considered other models in which the chromophore appeared in a vertically detached stratospheric haze, which did not fit as well, or as a coating on the particles of the main cloud layer, for which the fit was significantly worse.

Here we use the same VIMS data set, but extend the analysis to other cloud features and consider more varied vertical structures, showing that models using the same chromophore can fit much of the color variation that is normally seen over Jupiter's disk.

### 2. OBSERVATIONS

#### 2.1. VIMS instrumental characteristics

The VIMS instrument (Brown et al. 2004) provides two overlapping spectral channels covering the ranges from 0.3 to 1.05 μm (VIS) and from 0.86 to 5 μm (IR) with an effective pixel size of 0.5 milliradians on a side and a near-IR spectral resolution of approximately 15 nm (sampled at intervals of approximately 16 nm). The IR channel uses a linear detector to record a spectrum for a single spatial pixel, so that an image must be acquired by scanning the FOV across the target. The visual observations use a CCD matrix detector which records both spectral and spatial information simultaneously. The image of the target is focused on an entrance slit which is dispersed by a grating and focused on a two-dimension CCD detector array, recording spatial information along the slit direction but spectral information in the dispersion direction. In the normal mode of operation on-chip summing is used to achieve a spectral resolution of 7.3 nm and a spatial resolution of 0.5 milliradians.

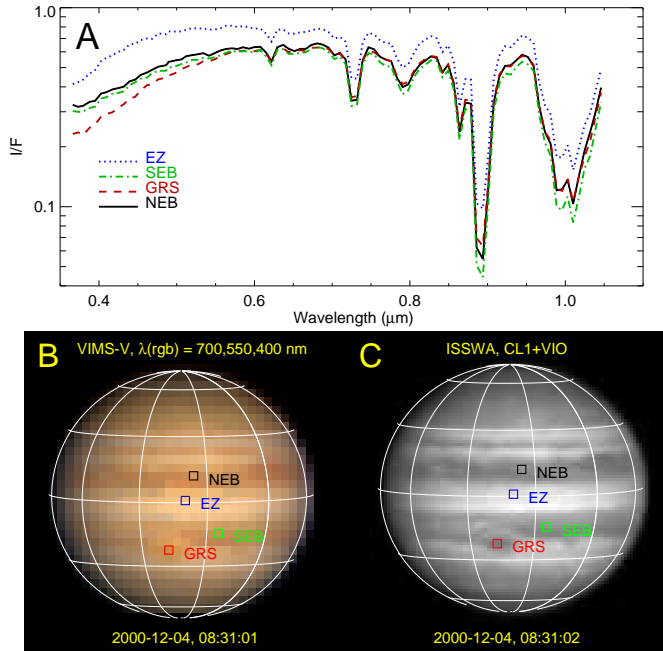


FIG. 1.— A: VIMS spectra from locations indicated in the VIMS image composite (B) and the ISS Violet-filtered image (C). The VIMS color composite image of Jupiter on 4 December 2000 used wavelength assignments given in the legend. The corresponding ISS image is nearly simultaneous with the VIMS observation. The grids are spaced  $30^\circ$  in planetocentric latitude and longitude. Over-plotted squares indicate locations of spectral samples used to characterize the GRS (red, dashed), SEB (green, dot-dash), EZ (blue, dotted) and NEB (black, solid).

### 2.2. Cassini VIMS observations of Jupiter.

In December 2000, the Cassini spacecraft passed near Jupiter for a gravitational assist on its journey to Saturn. During the flyby it observed Jupiter using a suite of instruments that included VIMS, which provided spectral observations of Jupiter’s atmosphere under conditions summarized in Table 1. The spatial resolution of the observations is limited by the rather large distance of the flyby. The low phase angle image acquired on 4 December is well suited for comparison with groundbased observations that provide a verification of the VIMS calibration at CCD wavelengths, but has relatively low spatial resolution. Images extracted from this data set and spectral samples at key locations can be seen in Fig. 1. The two observations at intermediate phase angles, from 31 December and 2 January, have much better spatial resolutions and provide two different observing geometries of the GRS and other cloud features, yielding additional constraints on radiative transfer models. Example images and spectral samples from these later data are provide in Fig. 2

### 2.3. VIMS Calibration and Navigation

The VIMS data set we used was reduced and calibrated using the USGS ISIS3 (Anderson et al. 2004) vimsal program, which was derived from the software provided by the VIMS team (and is available on PDS archive volumes), and uses the same calibration files and solar spectrum. A sanity check on the calibration was obtained by computing a disk average spectrum from the low-phase angle VIMS cube and comparing it with disk-averaged observations of Karkoschka (1998) taken in 1995 and

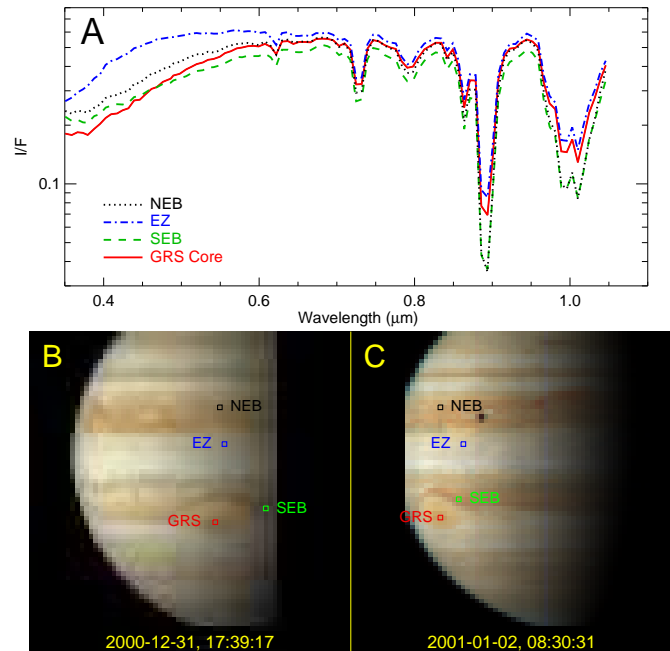


FIG. 2.— A: Spectral samples from VIMS image cube V1357116132\_1 (from which the color composite in C was made). B: color composite image from VIMS cube V1356976257\_3, taken when features in C were positioned closer to the terminator. The wavelengths used for blue, green, and red channels in the composite images are 450, 550, and 750 nm, respectively. The locations of spectral samples are indicated by colored squares and labels. Observation C was made 38.85 hours after observation B. Samples in the second cube were acquired at positions as close as possible to the predicted locations of features shown in B, accounting for drift due to Jupiter’s zonal wind profile. The dark pixel in image C (below the B in NEB) is due to the transit of Europa.

1993. The results, shown in Fig. 3, are plausibly consistent within 10%, given the the time difference between the two observations sets. A more contemporaneous calibration check is provided by Cassini ISS band-pass filtered images of the type shown in Fig. 1B, which provide comparisons at discrete wavelength bands, as shown in Fig. 3B. The ISS calibration leads to I/F values that are 20% greater than produced with the VIMS calibration. Given that the ISS calibration is being revised to put it into better agreement with the Karkoschka ground-based observations, we also considered Hubble Space Telescope WFPC2 observations obtained on 14 October 1999 as another sanity check. Unfortunately, most of those WFPC2 observations were overexposed, partially saturated, and not usable for disk-integrated comparisons. Three images that were not saturated (using filters F410M, F673N, and F953N) produced disk-integrated I/F values that are compared with VIMS in Fig. 3B. Given that the F410M and F673N images have the most reliable calibration, we interpret these results to mean that the HST WFPC2 calibration leads to I/F values about 10% higher than the VIMS results, which is close to the 12% higher values we estimated for the Karkoschka groundbased calibration. As the HST results are only about 14 months earlier than the VIMS observations in question, while the Karkoschka measurements were 5 and 7 years earlier, that they lead to essentially the same disk-averaged results suggests that Jupiter’s disk-averaged reflectivity is likely stable within about the 4% uncertainty claimed for the Karkoschka measurements.

TABLE 1  
SUMMARY OF VIMS OBSERVATIONS USED IN OUR ANALYSIS.

| VIMS-VIS Cube:             | V1354610545_3  | V1356976257_3   | V1357116132_1   |
|----------------------------|----------------|-----------------|-----------------|
| Date                       | 2000-12-04     | 2000-12-31      | 2001-01-02      |
| Time (UT)                  | 08:31:02       | 17:39:17        | 08:30:31        |
| Obs. Name: VIMS_C23JU_+    | 6ATM2X2163_ISS | ATMOS02A000_ISS | FEATURE005_CIRS |
| Sampling Mode              | HI-RES         | HI-RES          | HI-RES          |
| Sun-Jupiter Distance (AU)  | 5.0379         | 5.0460          | 5.0464          |
| Phase Angle                | 9.76°          | 67.83°          | 76.77°          |
| S/C-Jupiter Range (km)     | 26,439,177     | 9,873,972       | 10,185,177      |
| Sub-observer Lat (centric) | 3.626°         | -0.283°         | -0.869°         |
| Sub-observer Lon (east)    | 318.506°       | 321.962°        | 1.719°          |
| Sub-solar Lat (centric)    | 2.948°         | 2.901°          | 2.898°          |
| Sub-solar Lon (east)       | 328.254°       | 254.185°        | 285.016°        |
| GRS emission cosine        | 0.8878         | 0.8766          | 0.48420         |
| GRS incidence cosine       | 0.8648         | 0.5707          | 0.8518          |
| GRS azimuth                | 160.48°        | 71.61°          | 65.67°          |

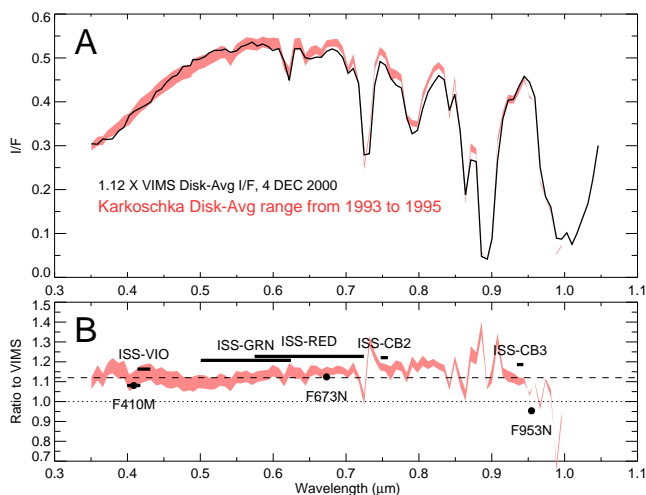


FIG. 3.— **A**: Disk-averaged I/F of Jupiter based on VIMS observations in December 2000 (solid curve, which is scaled by a factor of 1.12) compared to groundbased measurements in July 1993 (Karkoschka 1994) and July 1995 (Karkoschka 1998) which are shown by a red band covering the range of the two groundbased measurements. **B**: Ratios to the VIMS spectrum of Karkoschka’s spectra, and to 14 December 1999 HST band-pass filter observations using F410M, F673N, and F953N filters, taken at a phase angle of 11.46°, and ISS band-pass filter images obtained within one hour of the VIMS observations. Karkoschka data were obtained at the European Southern Observatory, and Jupiter phase angles were 9.8° and 6.8°, respectively. Reference lines at ratios of 1.0 (dotted) and 1.12 (dashed) are also shown.

The net impact of these comparisons is that we should seriously consider raising the VIMS I/F by about 10%.

The navigation of the ISIS3-processed cubes had to be adjusted to correct pointing errors. That was done using limb fitting and cross checked with contemporaneous ISS wide-angle imaging observations.

### 3. RADIATIVE TRANSFER MODELING

#### 3.1. Atmospheric structure and composition

We used the tabulated results of Seiff et al. (1998) for Jupiter’s temperature structure down to the 22-bar level, and assumed a dry adiabatic extrapolation below 22 bars. We assumed an atmospheric composition of  $\text{He}/\text{H}_2=0.157\pm 0.003$  (von Zahn et al. 1998) and  $\text{CH}_4/\text{H}_2= 2.1\times 10^{-3}\pm 0.4\times 10^{-3}$  (Niemann et al. 1998), which are expressed as number density ratios. Because

$\text{NH}_3$  is a condensable gas and is vertically variable below the condensation level, as well as horizontally variable, we selected a parameterized profile that fit the observed spectrum. The parameterization is described in Sec. 3.2. We assumed that the hydrogen para fraction matched the local equilibrium value.

#### 3.2. $\text{NH}_3$ parameterization

We characterized the  $\text{NH}_3$  profile using three parameters listed in Table 2: a pressure break point  $p_1$ , a deep mixing ratio  $nh_3v_0$  for  $p > p_1$ , and a depleted mixing ratio  $nh_3v_1$  for  $p_c < p < p_1$ , where  $p_c$  is the condensation pressure. A sample profile is shown in the left panel of Fig. 4, which also displays profiles consistent with radio observations in the right panel. We assumed that  $\text{NH}_3$  is saturated above the condensation level, an arbitrary choice to which the visible spectra are not very sensitive. There is insufficient sensitivity to  $\text{NH}_3$  in the CCD spectral range to allow determination of all three profile parameters independently. It is well established that the  $\text{NH}_3$  mixing ratio increases with depth, based on radio observations (de Pater 1986; de Pater et al. 2016), as well as Galileo probe observations (Sromovsky et al. 1998; Folkner et al. 1998). What is less well defined is the nature of the transition between deep and upper tropospheric values, although it seems clear that belts are more depleted than zones and likely depleted to somewhat greater depths (de Pater 1986), as indicated in the right panel of Fig. 4. In view of this characteristic we decided to use a fixed value of  $4\times 10^{-4}$  for the deep mixing ratio, which is close to the Folkner et al. value at 6 bars (Fig. 4) and well within the range allowed by radio observations, and make the upper mixing ratio and transition pressure adjustable parameters constrained to minimize  $\chi^2$ . However, given the generally weak effect of these parameters on the observed CCD spectrum, these parameters cannot be tightly constrained.

#### 3.3. Gas absorption models

The importance of the various gas absorbers is indicated by the penetration depth profile in Fig. 5. The two-way unit optical depth level is shown individually for absorptions by methane (red), ammonia (cyan), and collision-induced absorption (gray). These are compared to the unit extinction optical depth level (2-way) for all

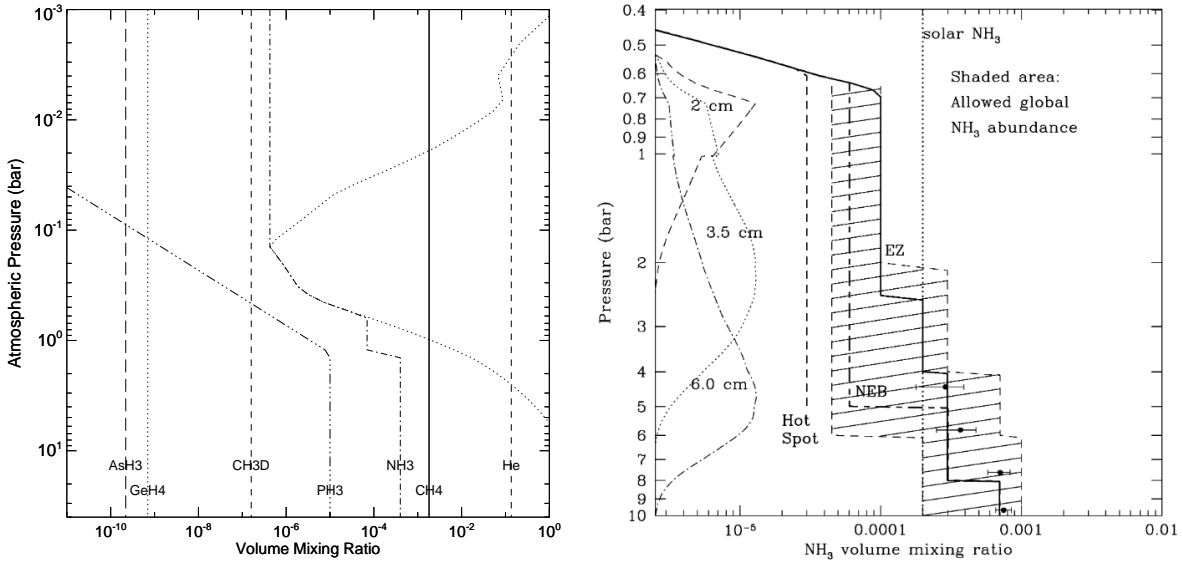


FIG. 4.— Left: Vertical gas profiles assumed in radiation transfer modeling. Only  $\text{NH}_3$ ,  $\text{CH}_4$ , and  $\text{H}_2$  have significant effects in the CCD spectral range, as indicated in Fig. 5. The  $\text{NH}_3$  profile is defined by adjustable parameters constrained to best fit  $\text{NH}_3$  spectral features. Right:  $\text{NH}_3$  volume mixing ratios consistent with radio observations, from Showman and de Pater (2005). The plotted points are from Folkner et al. (1998).

gas absorptions combined together with Rayleigh scattering extinction. Methane and ammonia are the dominant gases that shape the features in Jupiter’s visible (CCD) spectrum. The lesser role of ammonia absorption is illustrated by the comparison of model spectra with and without ammonia absorption that is shown in the top panel of Fig. 5.

Gas absorptions are all modeled using 10-term correlated- $k$  fits. For methane these are based on band models published by Karkoschka and Tomasko (2010) (we used P. Irwin’s fits, which are available at <http://users.ox.ac.uk/~atmp0035/ktables/> in compressed files `ch4_karkoschka_IR.par.gz` and `ch4_karkoschka_vis.par.gz`). Ammonia models are based primarily on Bowles et al. (2008) (in this case we used the fit described by Sromovsky and Fry (2010a)). Collision-induced absorption (CIA) for  $\text{H}_2$  and  $\text{H}_2$ -He was calculated using programs downloaded from the Atmospheres Node of the Planetary Data System, which are documented by Borysow (1991, 1993) for the  $\text{H}_2$ - $\text{H}_2$  fundamental band, Zheng and Borysow (1995) for the first  $\text{H}_2$ - $\text{H}_2$  overtone band, Brodbeck et al. (1999) for the second  $\text{H}_2$ - $\text{H}_2$  overtone band, and by Borysow (1992) for  $\text{H}_2$ -He bands. Where  $\text{CH}_4$  and  $\text{NH}_3$  gas absorptions overlap we compute opacities for 100 combinations of 10  $\text{CH}_4$  terms by 10  $\text{NH}_3$  terms and then sort and refit to a 10-term weighted sum.

### 3.4. Radiation Transfer Code

We used radiation transfer code based on that described by Sromovsky and Fry (2010a) and Sromovsky and Fry (2010b), with some enhancements and exceptions. The IR code was extended to CCD wavelengths so that correlated- $k$  models could be used at short wavelengths. Increased parallelism was added so that wavelengths as well as correlated- $k$  terms could be run in parallel. Our two-component coated-sphere particle scattering code is based on algorithms originated by Toon and Ackerman (1981).

We approximated the line-spread function of the VIMS instrument as a Gaussian of  $\text{FWHM} = 0.007 \mu\text{m}$ , then collected all the opacity values within  $\pm\text{FWHM}$  of the sample wavelength, weighted those according to the relative amplitude of the line-spread function, then sorted and refit to ten terms again.

We ignored both Raman scattering and polarization effects, based on comparing trial calculations including these effects with those that did not. For the crème brûlée model, Raman scattering had no noticeable effects beyond 370 nm, and including polarization depressed the I/F by a mean of only 0.8% and an RMS deviation of only 0.3%, both well below our estimated uncertainties. We used a model atmosphere with 57 layers between 0.5 mbar and 40 bars, with additional layers introduced to account for cloud pressure boundaries and the ammonia pressure break point appearing between our initial layer boundaries. We used 16 zenith angle quadrature points per hemisphere and 16 to handle azimuthal variations. Calculations with 12 quadrature points in each dimension had a maximum difference of only 0.03% of I/F, implying that 16 quadrature points per hemisphere were more than adequate.

## 4. PARAMETERIZATION OF CLOUD STRUCTURE AND OPTICAL PROPERTIES

### 4.1. Chromophore optical properties

The imaginary index and scattering properties of the Carlson et al. (2016) chromophore are displayed in Fig. 6. This material is nearly an order of magnitude more absorbing than the tholin measured by Khare et al. (1993), also shown for comparison. The imaginary index of the new material also has a nearly constant logarithmic slope over the 0.4-0.6  $\mu\text{m}$  wavelength range, which turns out to be a desirable feature in matching the visible spectra of Jovian clouds. Note the large change in slope of the tholin index in this range. Although Loeffler et al. (2016) did not measure the refractive index of the material they produced (created by irradiation of  $\text{NH}_4\text{SH}$ ),

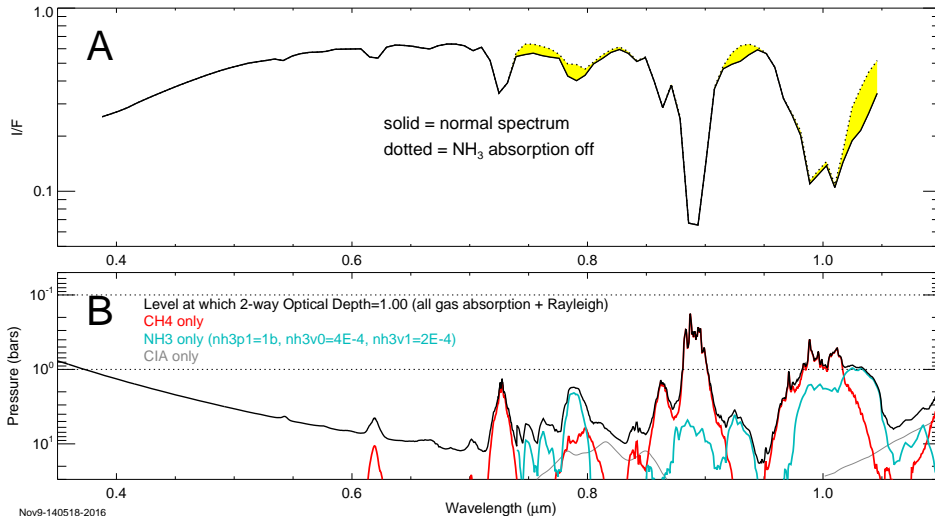


FIG. 5.— A: Model spectra with  $\text{NH}_3$  absorption included (solid) and without (dotted), with the difference colored yellow. B: Pressure at which 2-way optical depth reaches unity vs wavelength for individual gases and for all gases combined, assuming a methane mixing ratio of  $\text{CH}_4/\text{H}_2 = 2.1 \times 10^{-3}$  the ammonia profile parameters are given in the legend.

the reflectivity they measured (reproduced in panel A) contains substantial slope changes at  $0.43 \mu\text{m}$  and  $0.5 \mu\text{m}$  that are not typical of the Jovian cloud spectra shown in Figs. 1 and 2. The scattering properties of pure chromophore particles, shown in panels B-D, assume a real index of  $n=1.4$ , following Carlson et al. (2016). These panels show imaginary index, single-scattering albedo, and extinction efficiency, all for particles made entirely of chromophore material and for particle radii from  $0.1$  to  $1.0 \mu\text{m}$ . In panel B the measured index is indicated using a thick solid line and the extrapolated values indicated by a thin dotted line. Note the dramatic spectral variations possible in scattering parameters obtained by changes in particle radius. This shows that small changes in particle size can have a dramatic impact on the color of light transmitted by a layer of such particles.

#### 4.2. Cloud model structure

The cloud model we used to reproduce the observed VIMS visual channel spectra is a relatively simple one, containing three layers of Mie-scattering spherical particles. Our parameterization is summarized in Table 2. The particles were assumed to have gamma size distributions (Hansen and Travis 1974) with variance parameter  $b = 0.1$ . The top layer is a stratospheric haze defined by an effective pressure  $p_1$ , a  $1\text{-}\mu\text{m}$  optical depth  $\tau_1$ , an effective particle size  $r_1$ , and a refractive index  $n_1(\lambda)$ . This layer is treated as a sheet cloud arbitrarily placed at 40 mbar. Its effect is found to be too small to reasonably constrain its vertical distribution. The next layer is the main cloud, which is parameterized by top pressure  $p_{2T}$  and bottom pressure  $p_2$ , a particle radius  $r_2$ , refractive index  $n_2(\lambda)$ , and optical depth  $\tau_2$ . For what Baines et al. (2016) called the *crème brûlée* model, which is the model we use in this analysis, there is a third layer tacked onto the top of the main layer. This third layer contains the red chromophore and is characterized by its optical depth  $\tau_3$  and particle radius  $r_3$ , as well as its refractive index  $n_3(\lambda)$ , which is taken from Carlson et al. (2016).

Because our model treats the main cloud layer as conservative, it is not an effective barrier to  $5\text{-}\mu\text{m}$  emission from deeper layers of Jupiter’s atmosphere. While

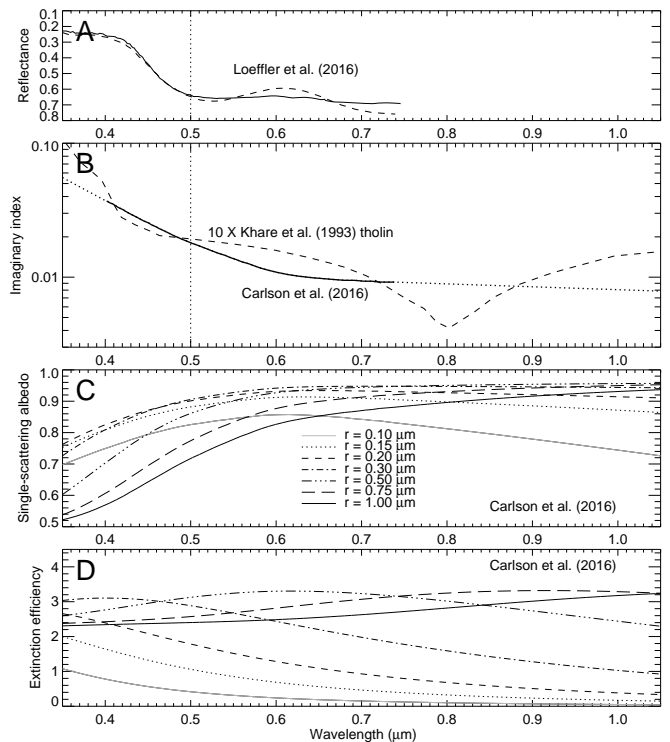


FIG. 6.— Chromophore imaginary index (B), single-scattering albedo (C), and extinction efficiency (D), all for particle sizes from  $0.1 \mu\text{m}$  to  $1.0 \mu\text{m}$ , assuming a gamma size distribution with  $b = 0.1$ . In (B) the Carlson et al. (2016) imaginary index measurement is displayed by the thick solid line and the assumed log-linear extrapolations are shown by the dotted line. The dashed line displays the tholin index of Khare et al. (1993) multiplied by a factor of ten. For reference, panel A displays the Loeffler et al. (2016) measurement of reflectivity of  $\text{NH}_4\text{SH}$  irradiated at a temperature of 120 K and warmed to a temperature of 190 K (dashed) and 200 K (solid). The y-axis scale in A is inverted so that increasing absorption is in the same sense (upward) as the refractive index plots in panel B.

that layer is not important in shaping the CCD portion of Jupiter’s reflection spectrum, it leaves the emission blocking to some deeper cloud layer that is not included here. Alternatively, one could add a small amount of

absorption to the main cloud layer so that it could do much, or even all, of the thermal blocking. However, that absorption is not needed to fit the visible spectrum, and finding a cloud structure that matches both thermal and reflected sunlight is left for future work.

#### 4.3. Refractive index of main cloud layer

The main cloud layer is a strong absorber near  $3\ \mu\text{m}$ , and is likely composed of some mixture of  $\text{NH}_3$  and  $\text{NH}_4\text{SH}$  (Sromovsky and Fry 2010a,b). If dominated by  $\text{NH}_3$ , the real refractive index  $n_2$  would be near 1.4, while if predominantly  $\text{NH}_4\text{SH}$ , the main layer's index would be closer to 1.8. Sato et al. (2013) found a best-fit real refractive index of 1.85 for Jovian clouds in the equatorial zone, favoring the dominance of  $\text{NH}_4\text{SH}$  in that location. In our analysis we tried models with both  $n_2 = 1.4$  and  $n_2 = 1.85$ , finding that the Carlson et al. (2016) chromophore provides a good fit to Jupiter's varied colors in either case.

#### 4.4. Vertical location of chromophore particles

The thin chromophore layer of the *crème brûlée* model is bounded on the bottom by the pressure at the top of the main cloud layer  $p_{2T}$  and on the top by  $0.9 \times p_{2T}$ . The arbitrary thickness of  $0.1 \times p_{2T}$  ( $\sim 20$  mbar) is not well constrained by the observations. For the low phase-angle observations, it appears that the chromophore could be in the stratospheric haze, or on top of the main cloud, or as a diffuse haze extending above the main cloud. This is consistent with the results of Baines et al. (2016), who considered two additional models: (1) models in which the chromophore material was only in a stratospheric haze, and (2) models in which the chromophore was a coating on the main cloud particles. Because neither of those models produced fits as accurate as the *crème brûlée* model, we mainly used the *crème brûlée* model in our analysis. However, models with chromophores in the stratosphere still provided relatively good fits to the spectrum and it is not possible to rule out a vertically distributed chromophore.

#### 4.5. Sensitivity to model parameters.

For the GRS *crème brûlée* model, we computed derivatives of the spectrum with respect to the fitted parameters. The results are shown in Figs. 7 and 8 as fractional derivatives, i.e. the fractional rate of change of I/F with respect to the fractional change in each fitted parameter. For example, panel B of Fig. 7 shows that if the optical depth of the main cloud is increased by 10%, the I/F at  $1\ \mu\text{m}$  would be increased by about 8%, but hardly changed at all at  $0.4\ \mu\text{m}$ , where Rayleigh scattering provides a significant contribution. The importance of Rayleigh scattering can also be seen in panel C, from the fact that moving the top of the main cloud layer to higher pressure increases the I/F at the shortest wavelengths. In panel H, we see that a 10% increase in the optical depth of the chromophore layer would produce about a 9% decrease in I/F at  $0.4\ \mu\text{m}$ , while panel F shows that a 10% increase in the radius of the chromophore particles would produced more than double that increase in I/F at the shortest wavelengths and almost nothing at the longest wavelengths.

Note the strong similarity, but opposite sense, between the derivatives of the bottom pressure of the main cloud

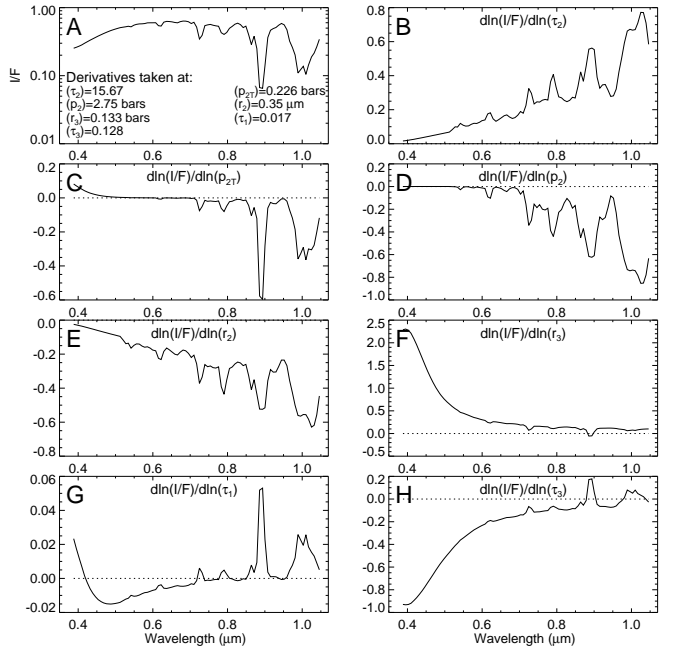


FIG. 7.— I/F spectrum (A) and derivatives of fractional changes in I/F with respect to fractional changes in parameters  $\tau_2$  (B),  $p_{2T}$  (C),  $p_2$  (D),  $r_2$  (E),  $r_3$  (F),  $\tau_1$  (G), and  $\tau_3$  (H).

(Fig. 7D) and the optical depth of the cloud (panel B). This arises because the most critical parameter controlling I/F is the density of the cloud near its top (optical depth per bar). If the optical depth is increased the I/F increases, more significantly at the longer wavelengths, but if the bottom pressure increases while the total optical depth is held fixed, then the optical depth per bar decreases throughout the cloud and then so does the I/F. This means that in fitting a spectrum, an increase in one requires an increase in the other to compensate, leading to a positive correlation in the fitting process, which has the value of 0.4433, as given in Table 3. The strongest correlation between fitted parameters (0.997) is actually between  $r_3$  and  $\tau_3$ . Note in panel C the strong effect of the main cloud's top pressure on the I/F near  $0.89\ \mu\text{m}$  and  $1.0\ \mu\text{m}$ , which implies that the observed I/F at these wavelengths provide a strong constraint on the cloud top pressure. The fractional derivatives with respect to the  $\text{NH}_3$  profile parameters (Fig. 8) are much weaker than most of the model parameters, typically yielding only a few percent change in I/F for a 10% parameter change. Note that the two gas parameters we chose to adjust have a roughly 50% correlation.

## 5. RESULTS FROM FITTING LOW PHASE ANGLE VIMS OBSERVATIONS.

### 5.1. Fit quality and parameter variations

Our initial fits to the low phase angle observations of the GRS showed that putting the chromophore in the stratospheric haze or at the top of the main cloud produce comparable and excellent fits. The model in which the chromophore appears as a coating on the main cloud particles provides an inferior fit. With the chromophore as a coating on all the particles in the main cloud, the UV-VIS reflectivity gradient of the model can't reach the observed gradient without making the longer wavelength

TABLE 2  
SUMMARY OF CLOUD AND NH<sub>3</sub> MODEL PARAMETERS USED IN SPECTRAL CALCULATIONS.

| Name, unit            | Description   | Value                                       |
|-----------------------|---|---|
| $p_1$ , bar           | stratospheric haze pressure                                 | 0.04-.07                                    |
| $r_1$ , $\mu\text{m}$ | stratospheric haze particle radius                          | fixed or adjustable                         |
| $\tau_1$              | stratospheric haze optical depth at 1 $\mu\text{m}$         | adjustable                                  |
| $n_1(\lambda)$        | stratospheric haze refractive index                         | $n_1 = 1.4 + 0i$ , or Carlson et al. (2016) |
| $p_{2T}$ , bar        | top of main cloud   | adjustable                                  |
| $p_2$ , bar           | bottom of main cloud  | adjustable                                  |
| $r_2$ , $\mu\text{m}$ | effective radius of main cloud particles                    | adjustable                                  |
| $\tau_2$              | optical depth of upper cloud at 1 $\mu\text{m}$             | adjustable                                  |
| $n_2(\lambda)$        | refractive index of main cloud                              | $n_2 = 1.4 + 0i$ or $n_2 = 1.85 + 0i$       |
| $p_{3T}$ , bar        | pressure at top of chromophore layer                        | normally = $p_{2T} \times 0.9$              |
| $p_3$ , bar           | pressure at base of chromophore layer                       | normally = $p_{2T}$                         |
| $r_3$ , $\mu\text{m}$ | effective radius of chromophore layer                       | adjustable                                  |
| $\tau_3$              | optical depth of chromophore layer at 1 $\mu\text{m}$       | adjustable                                  |
| $n_3(\lambda)$        | chromophore layer refractive index                          | Carlson et al. (2016)                       |
| $H_c/H_g$             | cloud particle to gas scale height ratio                    | normally = 1.0                              |
| $nh_{3v_0}$           | NH <sub>3</sub> vmr for $p > nh_{3p_1}$ (deep mixing ratio) | set to $4 \times 10^{-4}$                   |
| $nh_{3v_1}$           | NH <sub>3</sub> vmr for $nh_{3p_1} > p >$ condensation $p$  | adjustable                                  |
| $nh_{3p_1}$ , bar     | NH <sub>3</sub> break-point pressure                        | adjustable                                  |

NOTE: aerosol particles are assumed to have a gamma size distribution with variance parameter  $b = 0.1$ , with distribution function  $n(r) = \text{constant} \times r^{(1-3b)/b} e^{-r/ab}$ , where with  $a = r_{eff}$  and  $b =$  dimensionless variance, following Hansen and Travis (1974). Our model does not include a deep absorbing cloud that is needed to block thermal emission in the 5- $\mu\text{m}$  region of the spectrum.

TABLE 3  
SAMPLE CORRELATION MATRIX FOR CLOUD AND GAS ADJUSTABLE PARAMETERS FOR THE CRÈME BRÛLÉE MODEL FIT TO THE GRS SPECTRUM SHOWN IN FIG. 9.

|             | $p_2$   | $\tau_1$ | $\tau_2$ | $r_2$   | $p_{2T}$ | $r_3$   | $\tau_3$ | $nh_{3p_1}$ | $nh_{3v_1}$ |
|-------------|---------|----------|----------|---------|----------|---------|----------|-------------|-------------|
| $p_2$       | 1.0000  | -0.1265  | 0.4433   | 0.1450  | -0.3262  | 0.2556  | 0.2659   | -0.0617     | -0.2219     |
| $\tau_1$    | -0.1265 | 1.0000   | 0.3484   | 0.4322  | 0.8220   | -0.9265 | -0.9161  | -0.2114     | -0.1991     |
| $\tau_2$    | 0.4433  | 0.3485   | 1.0000   | 0.9394  | 0.2008   | -0.3994 | -0.4121  | 0.0040      | 0.2388      |
| $r_2$       | 0.1450  | 0.4323   | 0.9394   | 1.0000  | 0.2692   | -0.5463 | -0.5691  | 0.0929      | 0.3082      |
| $p_{2T}$    | -0.3262 | 0.8220   | 0.2007   | 0.2692  | 1.0000   | -0.7311 | -0.7088  | -0.3587     | -0.1306     |
| $r_3$       | 0.2556  | -0.9265  | -0.3994  | -0.5463 | -0.7311  | 1.0000  | 0.9969   | 0.1405      | 0.0840      |
| $\tau_3$    | 0.2660  | -0.9161  | -0.4121  | -0.5691 | -0.7089  | 0.9969  | 1.0000   | 0.1196      | 0.0658      |
| $nh_{3p_1}$ | -0.0617 | -0.2114  | 0.0041   | 0.0930  | -0.3587  | 0.1405  | 0.1196   | 1.0000      | 0.4977      |
| $nh_{3v_1}$ | -0.2219 | -0.1991  | 0.2388   | 0.3082  | -0.1306  | 0.0840  | 0.0658   | 0.4977      | 1.0000      |

continuum regions too dark. This results in an optimum core fraction of 0.96 of the total particle radius, or a coating fraction 0.04. This fits within in the range of coated sphere results given in the Carlson et al. (2016) paper, but does not yield a good fit to the observed spectral gradient, mainly due to Rayleigh scattering above the main cloud, which reduces the spectral gradient produced at the main cloud level.

The crème brûlée model fits to low phase angle spectra of GRS, SEB, EZ, and NEB cloud structures are shown in Fig. 9, where model spectra are shown as dotted lines in comparison with measured spectra, displayed with a light red band covering the uncertainty range assumed for measured and modeled spectra. Numeric values of the fitted model parameters and their uncertainties are given in Table 4. The fits are all roughly as good as might be expected given estimated uncertainties. For 91 wavelengths and 9 fitted parameters, we should expect  $\chi^2 \approx N_F = 91-9 = 82$ , within an uncertainty of  $\sqrt{2N_F} = 13$ .

Table 4 shows reduced  $\chi^2$  values ( $\chi^2/N_F$ ) from 0.98 to 1.22, which satisfy these expectations.

The main result of the fits for these very different cloud regions on Jupiter is that the different degrees of reddish colors they exhibit can all be accurately reproduced using the same chromophore described by Carlson et al. (2016), when placed in a thin layer on top of the main cloud layer, changing only the optical depth (from 0.13 for the GRS to 0.22 for the NEB) and the effective particle size (from 0.13  $\mu\text{m}$  for the GRS to 0.33  $\mu\text{m}$  for the NEB). *The Carlson et al. substance seems to be a nearly universal chromophore for modeling Jupiter's colors.*

## 5.2. Chromophore total mass loading

It is of some interest for models of production and evolution of the chromophore material to estimate the total mass of chromophore present per unit area in each of these cloud systems. Assuming a density of 1  $\text{g}/\text{cm}^3$ , and a single particle size instead of a distribution, the mass per unit area can be estimated as the number of

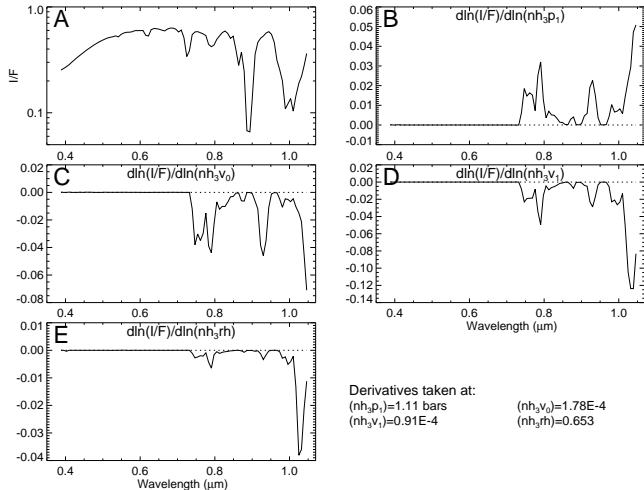


FIG. 8.— I/F spectrum (A) and fractional changes in I/F with respect to fractional changes in parameters  $nh_{3p1}$  (B),  $nh_{3v0}$  (C),  $nh_{3v1}$  (D), and  $nh_{3rh}$  (E), for conditions shown in the legend (from a model given in Table 4 that fits the low phase angle GRS core spectrum). These parameters generally have a much smaller effect on the spectrum than those shown in Fig. 7, where a fractional change in those parameters can produce roughly the same fractional change in parts of the I/F spectrum. Here the fractional changes in I/F are typically only 5-10% of the fractional parameter changes.

particles per unit area times the volume of each particle. As given in Table 4, the chromophore mass densities in units of  $\mu\text{g}/\text{cm}^2$  are 19 for the GRS, 18 for the SEB, 13 for the EZ, and 20 for the NEB. This is a remarkable degree of uniformity in the vertically integrated amount of coloring agent over such a wide range of vertical cloud structures, as illustrated in Fig. 10. If the chromophore is produced by a chemical process beginning with photolysis of ammonia, followed by chemical reactions with acetylene, the production must be occurring at least initially well above the cloud tops, where acetylene and ammonia abundances produce the maximum reaction rate. One would have thought that a production at low pressures, then the process of coagulation and sedimentation would result in a vertically distributed haze, rather than what seems to be the case here, namely a haze of very small scale height, plastered on top of the main cloud layer in each region. However, it is only for the GRS that we tested the possibility of an extended haze. Perhaps for the NEB and SEB, we might find a different result. The distributed haze was also not tested for scaled up I/F values, nor for high-index main cloud particles.

### 5.3. Effects of calibration and main cloud index variations

Table 5 summarizes the effects on fit-derived parameters for the NEB region due to changing the refractive index of the main cloud layer from 1.4 to 1.85, and the effects of multiplying the VIMS I/F observations by a factor of 1.12 before doing the model fitting. As evident from the reduced  $\chi^2$  values for these various cases, the effects on fit quality are minimal and differ so little from the nominal case that they do not warrant a comparison of the model spectra. No matter which value of  $n_2$  is chosen or which I/F calibration is chosen, a model structure can be found that yields an excellent fit to the observed spectra. Thus our conclusions that the Carlson et al.

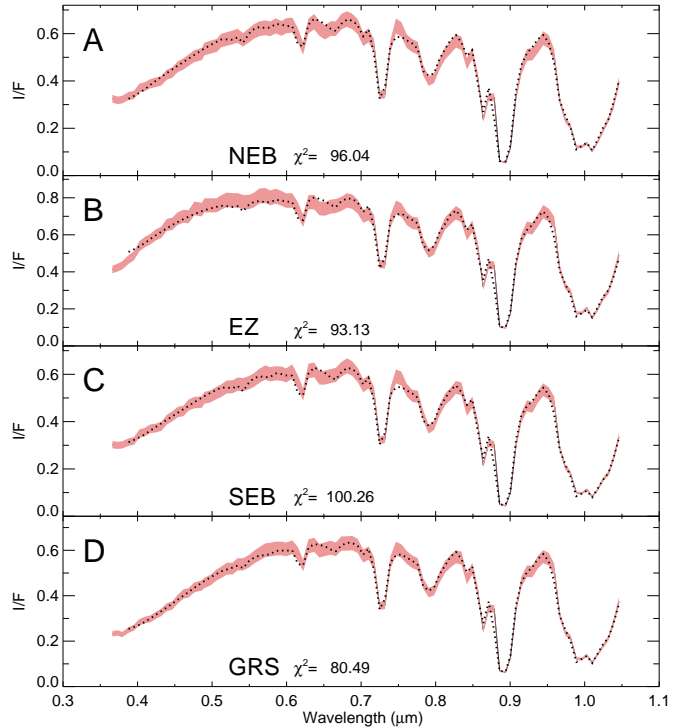


FIG. 9.— Crème brûlée model spectra (dotted lines) fitted to low phase angle measured spectral samples from NEB (A), GRS (B), EZ (C), and SEB (D), shown as pale red bands bounding the assumed uncertainty range for combined model and measurement errors. The best-fit values of the adjusted parameters are given in Table 4.

(2016) chromophore can be used to reproduce nearly any Jovian spectrum remains unaffected. The main effect of increasing the observed I/F by a factor of 1.12 is to produce modest increases in  $p_2$ , and  $\tau_2$ , slight decreases in  $p_{2T}$ ,  $r_2$ ,  $\tau_3$ , and  $nh_{3p1}$ , with almost no change in the remaining parameters. The refractive index changes are more significant: mainly a nearly 50% drop in  $\tau_2$  and a substantial decrease in  $r_2$ , with only modest decreases in  $nh_{3v1}$ . The fit quality differences are so slight as to provide no preference for either calibration or refractive index options.

## 6. RESULTS FROM FITTING MEDIUM PHASE ANGLE OBSERVATIONS.

As evident in Fig. 2, the medium phase angle observations from 31 December 2000 and 1 January 2001 offer the advantages of higher spatial resolution and two different viewing geometries that provide additional constraints on the vertical structure of clouds and hazes, as well as their scattering properties. By accounting for the zonal wind-induced drift of features during the 38.85 hours between the two observations, we are able to extract spectral samples from the same atmospheric region, although whether this represents the same cloud structure depends on whether it has evolved over that time interval. Thus, our constraint improvement is partly negated by the uncertain degree of structure evolution that might have taken place. There is also the possibility that eddy motions have altered the position of the feature from what we predicted using the assumption of a constant zonal wind speed. In addition, there is some uncertainty in the spectral sample due to the pixel quan-



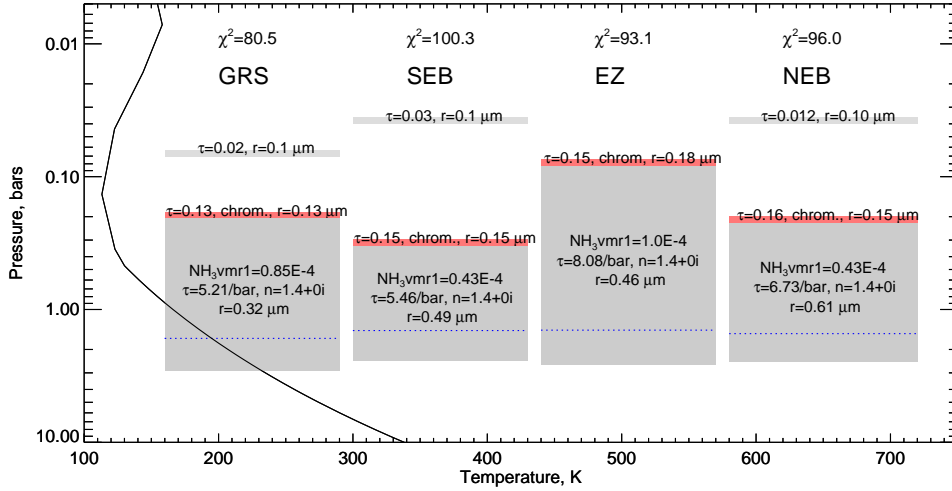


FIG. 10.— Crème brûlée cloud model fits to low phase-angle VIMS spectral samples from NEB, GRS, EZ, and SEB regions on Jupiter. The blue dotted line indicates the pressure below which the  $\text{NH}_3$  vmr is assumed to be  $4 \times 10^{-4}$ . Spectral fits are shown in Fig. 9. Adjusted parameter values and uncertainties are given in Table 4.

TABLE 4  
BEST-FIT PARAMETER VALUES FOR CRÈME BRÛLÉE MODEL FITS TO VIMS LOW PHASE-ANGLE OBSERVATIONS, USING  $nh_3p_1$  AND  $nh_3v_1$  AS ADJUSTABLE  $\text{NH}_3$  PROFILE PARAMETERS.

| Parameter, unit  | GRS (20.5° S)             | SEB (12.9° S)              | EZ (1.8° N)                | NEB (12.6° N)              |
|--|---------------------------|----------------------------|----------------------------|----------------------------|
| $\tau_1$   | $0.020^{+0.087}_{-0.017}$ | $0.027^{+0.019}_{-0.012}$  | $0.000^{+0.000}_{-0.000}$  | $0.012^{+0.076}_{-0.011}$  |
| $p_{2T}$ , bar   | $0.207^{+0.043}_{-0.036}$ | $0.330^{+0.045}_{-0.042}$  | $0.083^{+0.031}_{-0.016}$  | $0.222^{+0.049}_{-0.041}$  |
| $p_2$ , bar  | $2.923^{+0.343}_{-0.311}$ | $2.418^{+0.196}_{-0.179}$  | $2.624^{+0.270}_{-0.244}$  | $2.465^{+0.209}_{-0.191}$  |
| $\tau_2$   | $14.15^{+4.54}_{-3.48}$   | $11.407^{+2.141}_{-1.813}$ | $20.520^{+4.420}_{-3.683}$ | $15.109^{+1.786}_{-1.606}$ |
| $\tau_2/(p_2 - p_{2T})$ , optical depth/bar                | 5.21                      | 5.46                       | 8.07                       | 6.74                       |
| $r_2$ , $\mu\text{m}$                                      | $0.321^{+0.101}_{-0.065}$ | $0.487^{+0.132}_{-0.098}$  | $0.463^{+0.100}_{-0.078}$  | $0.611^{+0.129}_{-0.105}$  |
| $r_3$ , $\mu\text{m}$                                      | $0.133^{+0.016}_{-0.014}$ | $0.145^{+0.013}_{-0.012}$  | $0.180^{+0.019}_{-0.018}$  | $0.217^{+0.013}_{-0.013}$  |
| $\tau_3$   | $0.128^{+0.035}_{-0.028}$ | $0.146^{+0.031}_{-0.026}$  | $0.154^{+0.000}_{-0.000}$  | $0.330^{+0.050}_{-0.046}$  |
| $\tau_3/(\pi r_3^2 Q_{\text{ext}})$ , part./ $\text{cm}^2$ | $1.90 \times 10^9$        | $1.40 \times 10^9$         | $5.23 \times 10^8$         | $4.67 \times 10^8$         |
| mass density, $\mu\text{g}/\text{cm}^2$                    | 18.81                     | 18.04                      | 12.82                      | 20.03                      |
| $nh_3p_1$ , bar  | $1.650^{+1.170}_{-0.590}$ | $1.440^{+0.410}_{-0.280}$  | $1.430^{+1.240}_{-0.508}$  | $1.520^{+0.520}_{-0.340}$  |
| $nh_3v_1 \times 10^4$                                      | $0.849^{+0.301}_{-0.235}$ | $0.432^{+0.143}_{-0.110}$  | $1.020^{+0.520}_{-0.393}$  | $0.426^{+0.177}_{-0.128}$  |
| $\chi^2$   | 80.49                     | 100.26                     | 93.13                      | 96.04                      |
| $\chi^2/N$   | 0.98                      | 1.22                       | 1.14                       | 1.17                       |

Note: Latitudes in column headings are planetocentric. The  $\text{NH}_3$  mixing ratio was set to  $nh_3v_0 = 4 \times 10^{-4}$  for  $p > p_1$ .

tization of the image, as well as errors in navigation. A partial assessment of whether our initial assumption that the structure has not changed is true or not can be made by comparing the fit quality obtained from fitting just one of the spectra to that obtained from fitting both simultaneously. For this purpose we would compare the reduced  $\chi^2$  values for each alternative. In most cases it appears that fit quality is not seriously degraded by forcing the model to fit both observations simultaneously.

The crème brûlée models that were fit to both spectral samples simultaneously produced spectra that are shown in Fig. 11 in comparison with the measured spectra, using the same style as shown for the low phase angle observations. The parameter values derived from these fits can be found in Table 6. Similar fits assuming  $n_2=1.85$  yield results given in Table 7. These are all very good fits,

although the NEB and SEB spectra are not as well fit as the GRS and EZ spectra. This pattern was also seen in the low phase angle observations, but differences in reduced  $\chi^2$  values were much smaller between different regions. It is conceivable that the deeper cloud structure of the NEB and SEB regions of Jupiter might mean that the cloud top is actually deeper than the chromophore layer, and that perhaps the crème brûlée model is not the most appropriate model for these regions. However, when we fit the spectra from just a single viewing geometry (Table 8), we don't see nearly as much difference between the different regions. In fact, the reduced  $\chi^2$  values more closely resemble those obtained from the low phase angle observations, as given in Table 4. The difference thus might be less due to problems with the model structure and more due to sampling problems. In the next subsec-

TABLE 5  
BEST-FIT PARAMETER VALUES FOR CRÈME BRÛLÉE MODEL FITS TO VIMS LOW PHASE-ANGLE OBSERVATIONS, WITH DIFFERENT CHOICES FOR SCALE FACTOR AND  $n_2(\lambda)$ .

| Parameter, unit   | $n_2 = 1.4 + 0i$<br>scale=1.0             | $n_2 = 1.4 + 0i$<br>scale=1.12             | $n_2 = 1.85 + 0i$<br>scale=1.0            | $n_2 = 1.85 + 0i$<br>scale=1.12           |
|---|---|--|---|---|
| $\tau_1$  | 0.012 <sup>+0.076</sup> <sub>-0.011</sub> | 0.000 <sup>+0.000</sup> <sub>-0.000</sub>  | 0.000 <sup>+0.000</sup> <sub>-0.000</sub> | 0.000 <sup>+0.000</sup> <sub>-0.000</sub> |
| $p_{2T}$ , bar  | 0.222 <sup>+0.049</sup> <sub>-0.041</sub> | 0.196 <sup>+0.029</sup> <sub>-0.025</sub>  | 0.233 <sup>+0.030</sup> <sub>-0.027</sub> | 0.228 <sup>+0.030</sup> <sub>-0.027</sub> |
| $p_2$ , bar   | 2.465 <sup>+0.209</sup> <sub>-0.191</sub> | 2.825 <sup>+0.268</sup> <sub>-0.246</sub>  | 2.624 <sup>+0.225</sup> <sub>-0.207</sub> | 2.993 <sup>+0.298</sup> <sub>-0.276</sub> |
| $\tau_2$  | 15.11 <sup>+1.79</sup> <sub>-1.61</sub>   | 17.390 <sup>+3.803</sup> <sub>-3.153</sub> | 6.809 <sup>+0.436</sup> <sub>-0.410</sub> | 9.680 <sup>+0.923</sup> <sub>-0.844</sub> |
| $\tau_2/(p_2 - p_{2T})$ , optical depth/bar                 | 6.74                                      | 6.61                                       | 2.85                                      | 3.50                                      |
| $r_2$ , $\mu\text{m}$                                       | 0.611 <sup>+0.129</sup> <sub>-0.105</sub> | 0.450 <sup>+0.100</sup> <sub>-0.077</sub>  | 0.325 <sup>+0.028</sup> <sub>-0.024</sub> | 0.296 <sup>+0.031</sup> <sub>-0.026</sub> |
| $r_3$ , $\mu\text{m}$                                       | 0.217 <sup>+0.013</sup> <sub>-0.013</sub> | 0.213 <sup>+0.013</sup> <sub>-0.013</sub>  | 0.220 <sup>+0.012</sup> <sub>-0.012</sub> | 0.212 <sup>+0.013</sup> <sub>-0.013</sub> |
| $\tau_3$  | 0.330 <sup>+0.050</sup> <sub>-0.046</sub> | 0.293 <sup>+0.034</sup> <sub>-0.032</sub>  | 0.351 <sup>+0.035</sup> <sub>-0.033</sub> | 0.289 <sup>+0.034</sup> <sub>-0.032</sub> |
| $\tau_3/(\pi r_3^2 Q_{\text{ext}})$ , part./cm <sup>2</sup> | $4.67 \times 10^8$                        | $4.57 \times 10^8$                         | $4.64 \times 10^8$                        | $4.56 \times 10^8$                        |
| mass density, $\mu\text{g}/\text{cm}^2$                     | 20.03                                     | 18.38                                      | 20.86                                     | 18.22                                     |
| $nh_3 p_1$ , bar  | 1.520 <sup>+0.520</sup> <sub>-0.340</sub> | 1.460 <sup>+0.140</sup> <sub>-0.120</sub>  | 1.620 <sup>+0.490</sup> <sub>-0.340</sub> | 1.500 <sup>+0.130</sup> <sub>-0.120</sub> |
| $nh_3 v_1 \times 10^4$                                      | 0.426 <sup>+0.177</sup> <sub>-0.128</sub> | 0.436 <sup>+0.201</sup> <sub>-0.141</sub>  | 0.363 <sup>+0.134</sup> <sub>-0.100</sub> | 0.357 <sup>+0.186</sup> <sub>-0.124</sub> |
| $\chi^2$  | 96.04                                     | 87.03                                      | 90.49                                     | 89.28                                     |
| $\chi^2/N$  | 1.17                                      | 1.06                                       | 1.10                                      | 1.09                                      |

Note: Latitudes in column headings are planetocentric. The  $\text{NH}_3$  mixing ratio was set to  $nh_3 v_0 = 4 \times 10^{-4}$  for  $p > p_1$ . Measured I/F values were multiplied by scale prior to finding best-fit parameter values.

tion we further consider what constraints can be placed on the vertical structure of the chromophore haze itself.

### 6.1. Constraining the vertical location of the chromophores

When we allowed the thin layer of chromophore particles to be elevated above the main cloud layer, with the pressure allowed to be adjusted to minimize  $\chi^2$ , the result for the low phase angle NEB observation was that the pressure of the elevated haze was driven as close to the top of the main cloud as the range boundaries allowed. However, when we forced the chromophore to reside at 60 mbar instead of putting it at the top of the main cloud layer (near 200 mb), we got an excellent overall fit that was only slightly deviant at the shortest wavelengths where Rayleigh scattering is attenuated by the high chromophore layer. Moving the layer downward would provide a useful I/F boost that would improve the fit at short wavelengths.

Using the more constrained set of observations near the end of December, which provide two different viewing geometries, we got a more definitive result. When we put the chromophore into a diffuse stratospheric haze layer extending from the top of the main cloud upward, and then tried to find the optimum ratio of the scale height of that haze to the pressure scale height, the scale height dropped to the minimum value allowed. The implication is that the chromophore layer seems to fit best when it is very thin, and right on top of the main cloud layer.

Considering the GRS dual spectral observations at medium phase angle to be the most reliably located with respect to the target feature in both cases, we first tried to use those spectra to better constrain the haze of chromophores above the GRS. Using a detached haze of chromophores again, we tried to optimize the fit to the dual spectra with an additional parameter, namely the pres-

sure of the chromophore layer, in this case not fixing it to the top of main cloud layer but allowing it to move between 200 mbar and 40 mbar. The result was that the haze pressure was again forced to the maximum value allowed, which is so close to the top of the main cloud that we cannot really distinguish it from being in contact with the main cloud. In this case we did not provide for a stratospheric haze at 40 mbar that might provide a positive scattering contribution. So, perhaps the haze was partly forced downward to allow a short wavelength boost of Rayleigh scattering. However, when we added such a haze, we got essentially the same result. This is similar to the results of Baines et al. (2016). When they put the chromophore into a stratospheric haze at 40 mbar, their fit quality was worse, but not dramatically so ( $\chi^2/N$  increased from 0.92 to 1.2).

### 6.2. Ammonia fit results

The most consistent result from both low and high phase angle VIMS observations is that the  $\text{NH}_3$  VMR immediately below the condensation level is significantly higher in the GRS and EZ by about a factor of two than it is in the SEB and NEB. The latter values range from  $4.2 \times 10^{-5}$  to  $4.9 \times 10^{-5}$ , with an average of  $4.5 \times 10^{-5}$ , which corresponds to an ammonia condensation level near 585 mbar, which is well below the cloud tops for all regions, and also well above the cloud bottoms. So the part of the NEB cloud deeper than 585 mbar is most likely composed of  $\text{NH}_4\text{SH}$ , while the upper part of the cloud is likely a mix of  $\text{NH}_3$  and  $\text{NH}_4\text{SH}$ . Whether such a construct would fit the observations much better remains to be seen, but it is clear that our conclusions about the suitability of the Carlson et al. (2016) chromophore as a coloring agent on Jupiter would not be affected. There is less consistency and much more uncertainty in the depth at which the upper mixing ratio transitions to the deeper

TABLE 6  
BEST-FIT PARAMETER VALUES ASSUMING  $n_2=1.40$  FOR CRÈME BRÛLÉE MODEL FITS SIMULTANEOUSLY CONSTRAINED BY VIMS MEDIUM PHASE-ANGLE OBSERVATIONS FROM BOTH VIEWING GEOMETRIES SHOWN IN FIG. 2.

| Parameter, unit   | GRS (20.4° S)             | SEB (14.7° S)              | EZ (0.7° N)                | NEB (13.3° N)              |
|---|---------------------------|----------------------------|----------------------------|----------------------------|
| $\tau_1$  | $0.004^{+0.004}_{-0.002}$ | $0.027^{+0.003}_{-0.003}$  | $0.000^{+0.000}_{-0.000}$  | $0.010^{+0.004}_{-0.003}$  |
| $p_{2T}$ , bar  | $0.205^{+0.012}_{-0.012}$ | $0.489^{+0.018}_{-0.018}$  | $0.060^{+0.034}_{-0.011}$  | $0.381^{+0.017}_{-0.017}$  |
| $p_2$ , bar   | $4.192^{+0.630}_{-0.614}$ | $4.900^{+0.703}_{-0.741}$  | $2.154^{+0.151}_{-0.138}$  | $3.213^{+0.243}_{-0.230}$  |
| $\tau_2$  | $29.56^{+4.24}_{-3.76}$   | $25.187^{+4.179}_{-3.631}$ | $13.663^{+1.348}_{-1.232}$ | $16.061^{+1.057}_{-0.995}$ |
| $\tau_2/(p_2 - p_{2T})$ , optical depth/bar                 | 7.41                      | 5.71                       | 6.52                       | 5.67                       |
| $r_2$ , $\mu\text{m}$                                       | $1.148^{+0.277}_{-0.245}$ | $0.836^{+0.239}_{-0.193}$  | $0.586^{+0.066}_{-0.059}$  | $1.438^{+0.220}_{-0.213}$  |
| $r_3$ , $\mu\text{m}$                                       | $0.149^{+0.007}_{-0.007}$ | $0.286^{+0.014}_{-0.015}$  | $0.117^{+0.014}_{-0.012}$  | $0.151^{+0.010}_{-0.009}$  |
| $\tau_3$  | $0.209^{+0.021}_{-0.020}$ | $0.757^{+0.058}_{-0.064}$  | $0.059^{+0.012}_{-0.010}$  | $0.186^{+0.023}_{-0.021}$  |
| $\tau_3/(\pi r_3^2 Q_{\text{ext}})$ , part./cm <sup>2</sup> | $1.79 \times 10^9$        | $3.18 \times 10^8$         | $1.70 \times 10^9$         | $1.49 \times 10^9$         |
| mass density, $\mu\text{g}/\text{cm}^2$                     | 24.71                     | 31.15                      | 11.34                      | 21.46                      |
| $nh_3p_1$ , bar   | $1.950^{+1.580}_{-0.840}$ | $2.020^{+0.590}_{-0.460}$  | $1.280^{+0.140}_{-0.120}$  | $2.180^{+0.800}_{-0.610}$  |
| $nh_3v_1 \times 10^4$                                       | $0.988^{+0.382}_{-0.302}$ | $0.449^{+0.103}_{-0.085}$  | $0.703^{+0.477}_{-0.308}$  | $0.494^{+0.093}_{-0.080}$  |
| $\chi^2$  | 159.12                    | 243.68                     | 195.52                     | 255.70                     |
| $\chi^2/N$  | 0.97                      | 1.49                       | 1.19                       | 1.56                       |

NOTE: Latitudes in column headings are planetocentric.  $\text{NH}_3$  mixing ratio  $nh_3v_1$  and pressure  $nh_3p_1$  were derived assuming  $nh_3v_0 = 4 \times 10^{-4}$ .

TABLE 7  
BEST-FIT PARAMETER VALUES ASSUMING  $n_2=1.85$  FOR CRÈME BRÛLÉE MODEL FITS SIMULTANEOUSLY CONSTRAINED BY VIMS MEDIUM PHASE-ANGLE OBSERVATIONS FROM BOTH VIEWING GEOMETRIES SHOWN IN FIG. 2.

| Parameter, unit   | GRS (20.4° S)             | SEB (14.7° S)              | EZ (0.7° N)                | NEB (13.5° N)             |
|---|---------------------------|----------------------------|----------------------------|---------------------------|
| $\tau_1$  | $0.003^{+0.005}_{-0.002}$ | $0.026^{+0.003}_{-0.003}$  | $0.005^{+0.040}_{-0.004}$  | $0.005^{+0.014}_{-0.004}$ |
| $p_{2T}$ , bar  | $0.198^{+0.012}_{-0.011}$ | $0.486^{+0.018}_{-0.018}$  | $0.125^{+0.017}_{-0.014}$  | $0.270^{+0.013}_{-0.013}$ |
| $p_2$ , bar   | $3.887^{+0.493}_{-0.471}$ | $4.687^{+0.647}_{-0.663}$  | $2.826^{+0.208}_{-0.194}$  | $2.907^{+0.259}_{-0.240}$ |
| $\tau_2$  | $14.11^{+2.07}_{-1.82}$   | $10.857^{+2.001}_{-1.698}$ | $13.890^{+0.809}_{-0.766}$ | $8.190^{+0.811}_{-0.739}$ |
| $\tau_2/(p_2 - p_{2T})$ , optical depth/bar                 | 3.83                      | 2.58                       | 5.14                       | 3.11                      |
| $r_2$ , $\mu\text{m}$                                       | $0.416^{+0.063}_{-0.052}$ | $0.329^{+0.046}_{-0.037}$  | $0.988^{+0.049}_{-0.047}$  | $0.346^{+0.035}_{-0.030}$ |
| $r_3$ , $\mu\text{m}$                                       | $0.140^{+0.007}_{-0.007}$ | $0.286^{+0.013}_{-0.014}$  | $0.126^{+0.015}_{-0.013}$  | $0.278^{+0.016}_{-0.017}$ |
| $\tau_3$  | $0.181^{+0.016}_{-0.015}$ | $0.744^{+0.056}_{-0.061}$  | $0.063^{+0.015}_{-0.012}$  | $0.545^{+0.053}_{-0.053}$ |
| $\tau_3/(\pi r_3^2 Q_{\text{ext}})$ , part./cm <sup>2</sup> | $2.13 \times 10^9$        | $3.12 \times 10^8$         | $1.23 \times 10^9$         | $2.57 \times 10^8$        |
| mass density, $\mu\text{g}/\text{cm}^2$                     | 24.274                    | 30.603                     | 10.292                     | 23.168                    |
| $nh_3p_1$ , bar   | $2.010^{+2.020}_{-0.990}$ | $2.000^{+0.630}_{-0.470}$  | $1.170^{+2.740}_{-0.437}$  | $1.990^{+0.940}_{-0.630}$ |
| $nh_3v_1 \times 10^4$                                       | $1.150^{+0.600}_{-0.450}$ | $0.417^{+0.105}_{-0.085}$  | $2.010^{+1.360}_{-1.360}$  | $0.490^{+0.162}_{-0.125}$ |
| $\chi^2$  | 164.34                    | 240.53                     | 194.55                     | 180.40                    |
| $\chi^2/N$  | 1.00                      | 1.47                       | 1.19                       | 1.10                      |

NOTE: Latitudes in column headings are planetocentric.  $\text{NH}_3$  mixing ratio  $nh_3v_1$  and pressure  $nh_3p_1$  were derived assuming  $nh_3v_0 = 4 \times 10^{-4}$ .

mixing ratio. Pressures from 1.43 bars to 1.65 bars are inferred from the low phase angle observations, but the uncertainties are very large, about 0.3 bars in the direction of lower pressures and 0.4 to 0.5 bars in the direction of increasing pressure. The transition pressures for the high phase angle dual fits are larger, averaging 2.1 bars with somewhat larger uncertainties in both directions.

The ammonia mixing ratios immediately below the condensation level in the GRS average about  $9 \times 10^{-5}$  with uncertainties of about  $0.3\text{-}0.4 \times 10^{-5}$ . This corresponds to a condensation pressure near 634 mbar, also well below the cloud top and well above the cloud bot-

tom. Thus the GRS is likely of mixed composition as well, though a bigger fraction of the cloud is at higher altitudes relative to the SEB or NEB. The EZ has a sub-condensation mixing ratio comparable to or lower than that of the GRS, but transitions to the deep mixing ratio at a lower pressure.

#### 7. SPECULATION ON PHYSICAL MECHANISMS

Production of the Carlson et al. (2016) chromophore depends on UV flux, ammonia, and acetylene. Because ammonia falls off with altitude and UV flux increases with altitude it is expected that production of photolyzed

TABLE 8  
BEST-FIT PARAMETER VALUES ASSUMING  $n_2=1.40$  FOR CRÈME BRÛLÉE MODEL FITS TO JUST THE VIMS MEDIUM PHASE-ANGLE OBSERVATIONS FROM THE SINGLE OBSERVING GEOMETRY ON 31 DECEMBER 2000.

| Parameter, unit  | GRS (20.4° S)             | SEB (14.7° S)              | EZ (0.7° N)                | NEB (13.5° N)              |
|--|---------------------------|----------------------------|----------------------------|----------------------------|
| $\tau_1$   | $0.007^{+0.008}_{-0.004}$ | $0.022^{+0.003}_{-0.003}$  | $0.000^{+0.000}_{-0.000}$  | $0.021^{+0.010}_{-0.007}$  |
| $p_{2T}$ , bar   | $0.204^{+0.017}_{-0.015}$ | $0.443^{+0.021}_{-0.021}$  | $0.072^{+0.057}_{-0.016}$  | $0.383^{+0.028}_{-0.027}$  |
| $p_2$ , bar  | $3.996^{+0.964}_{-0.901}$ | $4.534^{+0.901}_{-0.912}$  | $2.656^{+0.338}_{-0.299}$  | $3.486^{+0.439}_{-0.409}$  |
| $\tau_2$   | $32.74^{+11.68}_{-8.89}$  | $22.311^{+4.504}_{-3.797}$ | $19.460^{+2.608}_{-2.318}$ | $18.837^{+2.014}_{-1.831}$ |
| $\tau_2/(p_2 - p_{2T})$ , optical depth/bar                | 8.63                      | 5.45                       | 7.53                       | 6.07                       |
| $r_2$ , $\mu\text{m}$                                      | $0.655^{+0.368}_{-0.234}$ | $2.365^{+0.066}_{-0.071}$  | $0.764^{+0.212}_{-0.169}$  | $1.201^{+0.328}_{-0.290}$  |
| $r_3$ , $\mu\text{m}$                                      | $0.137^{+0.017}_{-0.015}$ | $0.217^{+0.030}_{-0.029}$  | $0.117^{+0.036}_{-0.025}$  | $0.140^{+0.017}_{-0.015}$  |
| $\tau_3$   | $0.192^{+0.034}_{-0.030}$ | $0.492^{+0.101}_{-0.097}$  | $0.050^{+0.028}_{-0.018}$  | $0.159^{+0.032}_{-0.027}$  |
| $\tau_3/(\pi r_3^2 Q_{\text{ext}})$ , part./ $\text{cm}^2$ | $2.51 \times 10^9$        | $7.02 \times 10^8$         | $1.42 \times 10^9$         | $1.86 \times 10^9$         |
| mass density, $\mu\text{g}/\text{cm}^2$                    | 26.83                     | 29.94                      | 9.51                       | 21.27                      |
| $nh_3p_1$ , bar  | $2.050^{+0.590}_{-0.460}$ | $1.810^{+0.280}_{-0.240}$  | $1.130^{+0.940}_{-0.313}$  | $1.950^{+0.820}_{-0.530}$  |
| $nh_3v_1 \times 10^4$                                      | $0.868^{+0.542}_{-0.371}$ | $0.400^{+0.153}_{-0.112}$  | $0.703^{+0.847}_{-0.427}$  | $0.388^{+0.117}_{-0.092}$  |
| $\chi^2$   | 82.07                     | 97.94                      | 78.76                      | 103.60                     |
| $\chi^2/N$   | 1.00                      | 1.19                       | 0.96                       | 1.26                       |

NOTE: Latitudes in column headings are planetocentric. Locations of spectral samples are shown in Fig. 2A.  $\text{NH}_3$  mixing ratio  $nh_3v_1$  and pressure  $nh_3p_1$  were derived assuming  $nh_3v_0 = 4 \times 10^{-4}$  and  $nh_3rh = 1.0$ .

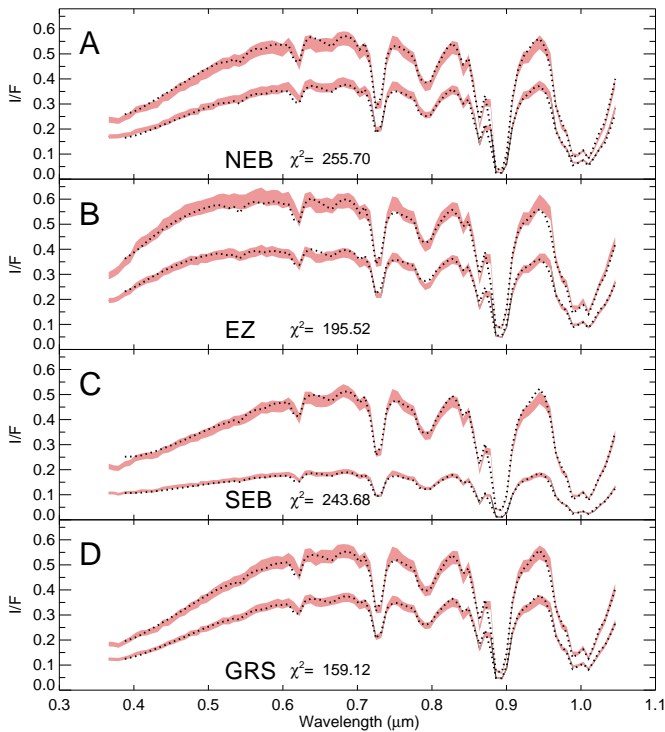


FIG. 11.— Crème brûlée model spectra for NEB (A), GRS (B), EZ (C), and SEB (D), shown as dotted lines compared to the medium phase angle measured spectra, displayed as light red bands bounding the assumed uncertainty range for combined model and measurement errors. In each panel the lower spectrum is from 31 December 2000 and the upper from 2 January 2001. For the selected features the larger incidence angle cosines in the January image produce brighter spectra in spite of the smaller emission angle cosines.

ammonia would occur somewhat above the cloud tops and would be widespread over Jupiter. The availability of acetylene seems to be a controlling factor in the production rate and its flux is quite weak on average according to current photochemical models (Moses et al. 2010). Baines et al. (2016) argued that lightning might raise the local acetylene mixing ratio sufficiently to produce the chromophore amounts needed at the top of the GRS. However, that argument would not work to explain the widespread distribution of the chromophore, as seems to be indicated by the close spectral matches we found over a number of different regions. An alternative suggested by Carlson et al. (2016) is that there may be an important photochemical role of ice grains and polyacetylene aerosols. If ammonia ice grains are important, that might explain why the chromophore seems to be located at the cloud tops (it might be produced there).

The variations we have seen in aerosol properties among different features, which are also at different latitudes, might have to do with stratospheric and/or upper tropospheric dynamics or differences in eddy mixing in the vicinity of the cloud tops. The biggest difference we have seen overall in chromophore mass loading is at the top of the Equatorial Zone, where we find about half the amounts seen in other regions. This might be evidence against the ice grain mechanism, considering that the cloud top is significantly higher and would be exposed to more UV flux, suggesting more production of chromophores than average, not less. This might be evidence instead for the gas phase production, because the ammonia mixing ratio above this high cloud feature would be less than average (assuming that ammonia is falling off with altitude at the same rate at all locations). However, both mechanisms depend on other factors such as eddy mixing differences that might work in the opposite direction. It remains to be determined whether there is a plausible mechanism to produce the chromophore

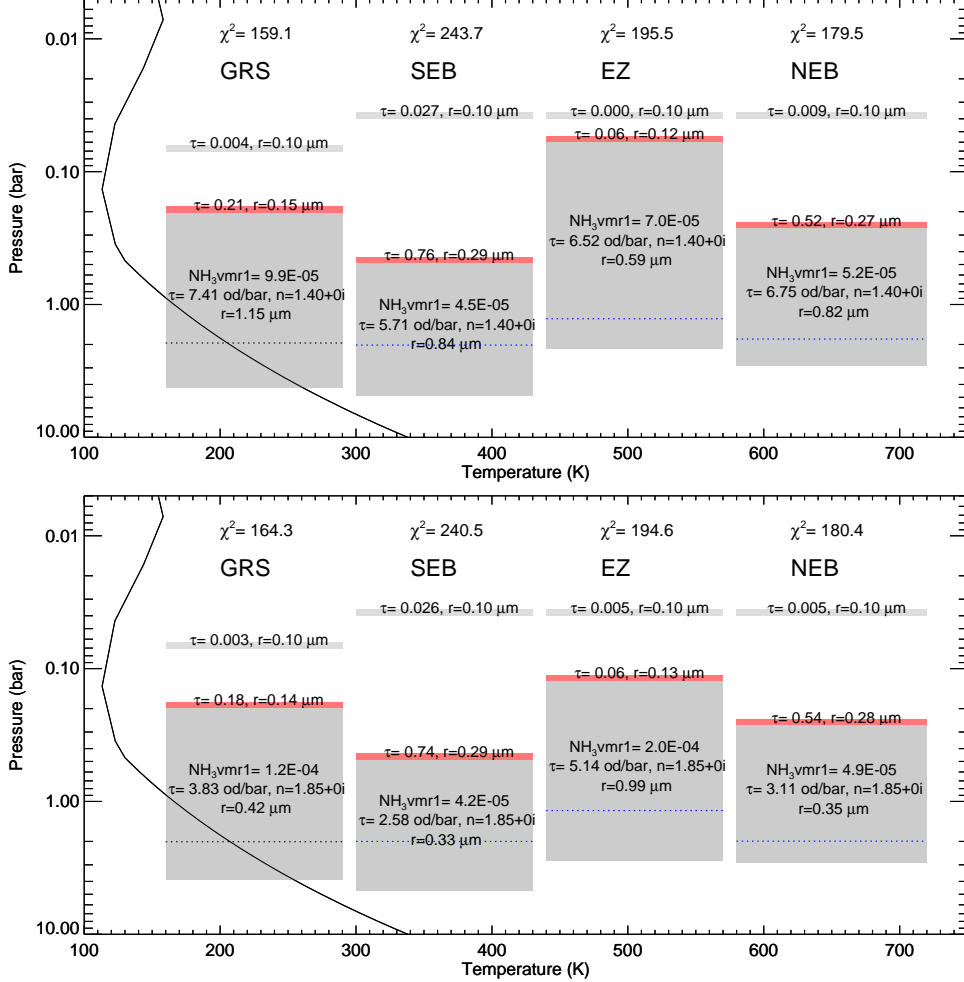


FIG. 12.— Crème brûlée cloud model fits to medium phase-angle VIMS spectral samples from NEB, GRS, EZ, and SEB regions on Jupiter, using constraints from both viewing geometries. The top panel is for  $n_2 = 1.4 + 0i$  and the bottom for  $n_2 = 1.85 + 0i$ . The higher index has the advantage of keeping the top of the main cloud in the equatorial zone below the temperature minimum. The blue dotted line indicates the pressure below which the  $\text{NH}_3$  vmr is assumed to be  $4 \times 10^{-4}$ . Spectral fits are shown in Fig. 9. Adjusted parameter values and uncertainties are given in Table 6 ( $n_2=1.4$ ) and Table 7 ( $n_2=1.85$ ).

amounts that are needed to match VIMS spectra and to explain the variations among different features. Photochemical models, microphysical models of cloud particle evolution, and dynamical models all seem needed to reach an understanding.

## 8. SUMMARY AND CONCLUSIONS

We used Jupiter’s 0.35–1.1  $\mu\text{m}$  spectrum, as measured by the Cassini/VIMS instrument near the end of 2000, to constrain cloud structures for the GRS, the equatorial zone, and north and south equatorial belts. We used a simple model structure in which the main cloud was composed of conservative particles and covered by a thin layer of particles made of the chromophore of Carlson et al. (2016). Our main conclusions from this investigation are as follows.

1. The substance described by Carlson et al. (2016) appears to be a universal chromophore for Jupiter’s clouds. Among the four cloud regions we studied with low phase angle observations, all have a reddish color that can be reproduced with the same kind of crème brûlée model that Baines et al.

(2016) used to model the GRS spectrum, i.e. a physically and optically thin layer immediately above the main cloud layer, with modest variations in particle size (from 0.13  $\mu\text{m}$  for the GRS to 0.22  $\mu\text{m}$  for the NEB) and, in all but one case, modest variations in 1- $\mu\text{m}$  optical depth (from 0.13 for the GRS to 0.33 for the NEB). For the medium phase angle observations, the range is similar except that the SEB spectrum in that data set led to the largest particle size (0.286  $\mu\text{m}$ ) and the largest optical depth (0.76).

2. The efficacy of the Carlson et al. (2016) chromophore in reproducing Jovian spectral colors is robust, even for 12% changes in VIMS calibration and large uncertainties in the refractive index of the main cloud layer due to uncertain fractions of  $\text{NH}_4\text{SH}$  and  $\text{NH}_3$  in its cloud particles.
3. Medium phase angle VIMS observations, which provided two different view and illumination angles of the same cloud regions, provide additional constraints on vertical structure, but add uncertainty due to the 38.5-hour time difference between

observations. Although these dual-angle fits produced about the same fit quality and similar properties of the chromophore layer, they yielded much larger particles for the main cloud layer (0.6 to 1.4  $\mu\text{m}$ , compared to 0.3-0.6  $\mu\text{m}$  obtained from the low phase angle observations).

4. According to the low phase angle observations, the vertically integrated masses of chromophore material above the GRS, SEB, EZ, and NEB are remarkably similar, ranging only from 13 to 20  $\mu\text{g}/\text{cm}^2$ , and only 18 to 20  $\mu\text{g}/\text{cm}^2$  if the EZ value is excluded. The range was somewhat larger for the medium phase angle results, ranging from 11

$\mu\text{g}/\text{cm}^2$  for the EZ to 21 – 31  $\mu\text{g}/\text{cm}^2$  for the other regions.

5. We also found a depression of the ammonia volume mixing ratio in the two belt regions, which averaged  $0.4\text{--}0.5 \times 10^{-4}$  immediately below the ammonia condensation level, while the other regions averaged twice that value.

#### ACKNOWLEDGMENTS

We thank Gordon Bjoraker and an anonymous reviewer for constructive reviews. LAS and PMF acknowledge support by NASA grant NNX14AH40G from NASA's Planetary Atmospheres Program.

#### REFERENCES

- Anderson, J. A., Sides, S. C., Soltesz, D. L., Sucharski, T. L., Becker, K. J., 2004. Modernization of the Integrated Software for Imagers and Spectrometers. In: Mackwell, S., Stansbery, E. (Eds.), *Lunar and Planetary Science Conference*. Vol. 35 of *Lunar and Planetary Science Conference*. p. 2039.
- Baines, K. H., Sromovsky, L. A., Carlson, R. W., Momary, T. W., Fry, P. M., 2016. The visual spectrum of Jupiter's Great Red Spot accurately modeled with aerosols produced by photolyzed ammonia reacting with acetylene. *Icarus* 000, submitted.
- Borysow, A., 1991. Modeling of collision-induced infrared absorption spectra of  $\text{H}_2\text{-H}_2$  pairs in the fundamental band at temperatures from 20 to 300 K. *Icarus* 92, 273–279.
- Borysow, A., 1992. New model of collision-induced infrared absorption spectra of  $\text{H}_2\text{-He}$  pairs in the 2-2.5 micron range at temperatures from 20 to 300 K - an update. *Icarus* 96, 169–175.
- Borysow, A., 1993. Erratum. *Icarus* 106, 614.
- Bowles, N., Calcutt, S., Irwin, P., Temple, J., 2008. Band parameters for self-broadened ammonia gas in the range 0.74 to 5.24  $\mu\text{m}$  to support measurements of the atmosphere of the planet Jupiter. *Icarus* 196, 612–624.
- Brodbeck, C., Bouanich, J.-P., van Thanh, N., Borysow, A., 1999. The binary collision-induced second overtone band of gaseous hydrogen: modelling and laboratory measurements. *Planet. Space Sci.* 47, 1285–1289.
- Brown, R. H., Baines, K. H., Bellucci, G., Bibring, J.-P., Buratti, B. J., Capaccioni, F., Cerroni, P., Clark, R. N., Coradini, A., Cruikshank, D. P., Drossart, P., Formisano, V., Jaumann, R., Langevin, Y., Matson, D. L., McCord, T. B., Mennella, V., Miller, E., Nelson, R. M., Nicholson, P. D., Sicardy, B., Sotin, C., 2004. The Cassini Visual and Infrared Mapping Spectrometer (VIMS) Investigation. *Space Sci. Rev.* 115, 111–168.
- Carlson, R. W., Baines, K. H., Anderson, M. S., Filacchione, G., Simon, A. A., 2016. Chromophores from photolyzed ammonia reacting with acetylene: Application to Jupiter's Great Red Spot. *Icarus* 274, 106–115.
- de Pater, I., 1986. Jupiter's zone-belt structure at radio wavelengths. II - Comparison of observations with model atmosphere calculations. *Icarus* 68, 344–365.
- de Pater, I., Sault, R. J., Butler, B., DeBoer, D., Wong, M. H., 2016. Peering through Jupiter's clouds with radio spectral imaging. *Science* 352, 1198–1201.
- Folkner, W. M., Woo, R., Nandi, S., 1998. Ammonia abundance in Jupiter's atmosphere derived from the attenuation of the Galileo probe's radio signal. *J. Geophys. Res.* 103, 22847–22856.
- Hansen, J. E., Travis, L. D., 1974. Light scattering in planetary atmospheres. *Space Sci. Rev.* 16, 527–610.
- Karkoschka, E., 1994. Spectrophotometry of the jovian planets and Titan at 300- to 1000-nm wavelength: The methane spectrum. *Icarus* 111, 174–192.
- Karkoschka, E., 1998. Methane, Ammonia, and Temperature Measurements of the Jovian Planets and Titan from CCD-Spectrophotometry. *Icarus* 133, 134–146.
- Karkoschka, E., Tomasko, M. G., 2010. Methane absorption coefficients for the jovian planets from laboratory, Huygens, and HST data. *Icarus* 205, 674–694.
- Khare, B. N., Thompson, W. R., Cheng, L., Chyba, C., Sagan, C., Arakawa, E. T., Meisse, C., Tuminello, P. S., 1993. Production and optical constraints of ice tholin from charged particle irradiation of (1:6)  $\text{C}_2\text{H}_6/\text{H}_2\text{O}$  at 77 K. *Icarus* 103, 290–300.
- Loeffler, M. J., Hudson, R. L., Chanover, N. J., Simon, A. A., 2016. The spectrum of Jupiter's Great Red Spot: The case for ammonium hydrosulfide ( $\text{NH}_4\text{SH}$ ). *Icarus* 271, 265–268.
- Moses, J. I., Visscher, C., Keane, T. C., Spier, A., 2010. On the abundance of non-cometary HCN on Jupiter. *Faraday Discussions* 147, 103.
- Niemann, H. B., Atreya, S. K., Carignan, G. R., Donahue, T. M., Haberman, J. A., Harpold, D. N., Hartle, R. E., Hunten, D. M., Kasprzak, W. T., Mahaffy, P. R., Owen, T. C., Way, S. H., 1998. The composition of the Jovian atmosphere as determined by the Galileo probe mass spectrometer. *J. Geophys. Res.* 103, 22831–22846.
- Sato, T. M., Satoh, T., Kasaba, Y., 2013. Retrieval of jovian cloud structure from the Cassini ISS limb-darkening data. I. Continuum scattering phase functions for cloud and haze in the South Tropical Zone. *Icarus* 222, 100–121.
- Seiff, A., Kirk, D. B., Knight, T. C. D., Young, R. E., Mihalov, J. D., Young, L. A., Milos, F. S., Schubert, G., Blanchard, R. C., Atkinson, D., 1998. Thermal structure of Jupiter's atmosphere near the edge of a 5- $\mu\text{m}$  hot spot in the north equatorial belt. *J. Geophys. Res.* 103, 22857–22890.
- Showman, A. P., de Pater, I., 2005. Dynamical implications of Jupiter's tropospheric ammonia abundance. *Icarus* 174, 192–204.
- Sromovsky, L. A., Collard, A. D., Fry, P. M., Orton, G. S., Lemmon, M. T., Tomasko, M. G., Freedman, R. S., 1998. Galileo probe measurements of thermal and solar radiation fluxes in the Jovian atmosphere. *J. Geophys. Res.* 103, 22929–22978.
- Sromovsky, L. A., Fry, P. M., 2010a. The source of 3- $\mu\text{m}$  absorption in Jupiter's clouds: Reanalysis of ISO observations using new  $\text{NH}_3$  absorption models. *Icarus* 210, 211–229.
- Sromovsky, L. A., Fry, P. M., 2010b. The source of widespread 3- $\mu\text{m}$  absorption in Jupiter's clouds: Constraints from 2000 Cassini VIMS observations. *Icarus* 210, 230–257.
- Toon, O. B., Ackerman, T. P., 1981. Algorithms for the calculation of scattering by stratified spheres. *Appl. Optics* 20, 3657–3660.
- von Zahn, U., Hunten, D. M., Lehmacher, G., 1998. Helium in Jupiter's atmosphere: Results from the Galileo probe helium interferometer experiment. *J. Geophys. Res.* 103, 22815–22830.
- West, R. A., Baines, K. H., Karkoschka, E., Sánchez-Lavega, A., 2009. Clouds and Aerosols in Saturn's Atmosphere. In: Dougherty, M. K., Esposito, L. W., Krimigis, S. M. (Eds.), *Saturn from Cassini-Huygens*. Springer, pp. 161–179.
- West, R. A., Strobel, D. F., Tomasko, M. G., 1986. Clouds, aerosols, and photochemistry in the Jovian atmosphere. *Icarus* 65, 161–217.
- Zheng, C., Borysow, A., 1995. Modeling of collision-induced infrared absorption spectra of  $\text{H}_2$  pairs in the first overtone band at temperatures from 20 to 500 K. *Icarus* 113, 84–90.